

# UC Irvine

## UC Irvine Previously Published Works

### Title

Depth-resolved birefringence and differential optical axis orientation measurements with fiber-based polarization-sensitive optical coherence tomography.

### Permalink

<https://escholarship.org/uc/item/88v556x8>

### Journal

Optics letters, 29(17)

### ISSN

0146-9592

### Authors

Guo, Shuguang  
Zhang, Jun  
Wang, Lei  
[et al.](#)

### Publication Date

2004-09-01

### DOI

10.1364/ol.29.002025

### Copyright Information

This work is made available under the terms of a Creative Commons Attribution License, available at <https://creativecommons.org/licenses/by/4.0/>

Peer reviewed

# Depth-resolved birefringence and differential optical axis orientation measurements with fiber-based polarization-sensitive optical coherence tomography

Shuguang Guo, Jun Zhang, Lei Wang, J. Stuart Nelson, and Zhongping Chen

Beckman Laser Institute, Department of Biomedical Engineering, University of California, Irvine, Irvine, California 92612

Received March 11, 2004

Conventional polarization-sensitive optical coherence tomography (PS-OCT) can provide depth-resolved Stokes parameter measurements of light reflected from turbid media. A new algorithm that takes into account changes in the optical axis is introduced to provide depth-resolved birefringence and differential optical axis orientation images by use of fiber-based PS-OCT. Quaternion, a convenient mathematical tool, is used to represent an optical element and simplify the algorithm. Experimental results with beef tendon and rabbit tendon and muscle show that this technique has promising potential for imaging the birefringent structure of multiple-layer samples with varying optical axes. © 2004 Optical Society of America

OCIS codes: 170.4500, 170.3880, 260.1440, 260.5430, 110.7050.

Optical coherence tomography (OCT), a noninvasive imaging technique for turbid media, uses coherence gating of the light source to obtain two- or three-dimensional images.<sup>1</sup> Polarization-sensitive OCT (PS-OCT) can provide additional information on the changes in light polarization states caused by birefringence, diattenuation of the sample, or both.<sup>2–10</sup> Conventional PS-OCT provides the overall phase retardation image, based on the assumption that the optical axis remains constant, as do the four Stokes parameter images of turbid media.<sup>4,6–8</sup> However, these images represent accumulated birefringence effects and do not represent the local structure of the sample. Recently, Jiao and Wang<sup>10</sup> developed differential phase retardation imaging to determine birefringence structure by calculating the absolute value of the retardation difference between two adjacent pixels. This algorithm is restricted by the assumption of a constant optical axis in the sample under study. An algorithm that takes into account changes in the optical axis, must be used to determine the depth-resolved birefringent structure if the sample is modeled with multiple-layer optics. In this Letter we present a new algorithm with a fiber-based PS-OCT system, which can resolve the problem when the optical axis changes as a function of depth and the polarization state changes within the fiber. The birefringence and differential optical axis orientation images are used to provide additional contrast for tissue structure.

To obtain the optical axis orientation and phase retardation, which varies with depth, the tissue and fiber are modeled with multiple-layer optics, with each layer considered a linear phase retarder, assuming there is no polarizer in the system. Such an optical system can be completely described as the rotation of three normalized Stokes parameters ( $S_1$ ,  $S_2$ , and  $S_3$  or  $Q$ ,  $U$ , and  $V$ ) by use of a Poincaré sphere representation. Jones and Mueller matrices are the most common mathematical tools used to represent an optical element. If absorption and diattenuation are negligible, there are only three independent parameters in Jones and Mueller matrices. In such cases, quaternion,

a more convenient mathematical tool introduced by Richartz and Hsu,<sup>11</sup> can be used to represent the optical element.

A rotation of an angle  $\omega$  about the axis  $(\cos \alpha_1, \cos \alpha_2, \cos \alpha_3)$ , where  $\cos^2 \alpha_1 + \cos^2 \alpha_2 + \cos^2 \alpha_3 = 1$ , can be described with a quaternion as  $\cos(\omega/2) + \sin(\omega/2)(\hat{i} \cos \alpha_1 + \hat{j} \cos \alpha_2 + \hat{k} \cos \alpha_3)$ ,<sup>11</sup> where  $\hat{i}$ ,  $\hat{j}$ , and  $\hat{k}$  are three imaginary units of a quaternion that satisfy  $\hat{i}^2 = \hat{j}^2 = \hat{k}^2 = \hat{i}\hat{j}\hat{k} = -1$ . Therefore the quaternion representation  $q_n$  of a linear phase retarder with a phase retardation of  $\Delta_n$  and an optical axis of  $\theta_n$  can be written as

$$q_n = \cos \frac{\Delta_n}{2} + \sin \frac{\Delta_n}{2} (\hat{i} \cos 2\theta_n + \hat{j} \sin 2\theta_n), \quad (1)$$

where subscript  $n$  represents the  $n$ th layer. The quaternion representation of multiple-layer linear phase retarders is the product of quaternions of individual retarders

$$q_n \cdots q_2 q_1 = a_n + \hat{i}b_n + \hat{j}c_n + \hat{k}d_n. \quad (2)$$

We express the polarization states of both forward and backscattered light in the forward coordinate system. With this convention the quaternion representation of a single linear phase retarder for backscattered light is identical to that of forward light. We use a lowercase letter  $q$  to represent the quaternion of a local layer and an uppercase letter  $Q$  to represent the accumulated quaternion. If Eq. (2) is considered the forward quaternion representation of multiple layers  $Q_{n,f}$ , the backscattered quaternion representation  $Q_{n,b}$  can be described as

$$Q_{n,b} = q_1 q_2 \cdots q_n = a_n + \hat{i}b_n + \hat{j}c_n - \hat{k}d_n. \quad (3)$$

The overall round-trip quaternion  $Q_{T,n}$  can be obtained as

$$\begin{aligned} Q_{T,n} &= Q_{\text{fiber},D} Q_{\text{fiber},S,b} Q_{n,b} Q_M Q_{n,f} Q_{\text{fiber},S,f} \\ &= A_n + \hat{i}B_n + \hat{j}C_n + \hat{k}D_n, \end{aligned} \quad (4)$$

where  $Q_M = 1$  is the quaternion of a mirror;  $Q_{\text{fiber},S,b}$ ,  $Q_{\text{fiber},S,f}$ , and  $Q_{\text{fiber},D}$  are quaternions of fibers in the sampling (backscattered and forward) and detection arms, respectively. Analogously, the overall round-trip quaternion of  $n + 1$  layers can be obtained as

$$\begin{aligned} Q_{T,n+1} &= Q_{\text{fiber},D} Q_{\text{fiber},S,b} Q_{n+1,b} Q_M Q_{n+1,f} Q_{\text{fiber},S,f} \\ &= A_{n+1} + \hat{i}B_{n+1} + \hat{j}C_{n+1} + \hat{k}D_{n+1}. \end{aligned} \quad (5)$$

Our goal is to obtain the phase retardation and optical axis orientation of the  $(n + 1)$ th layer. On the basis of Eqs. (1)–(5), the phase retardation of the  $(n + 1)$ th layer can be resolved as

$$\cos \Delta_{n+1} = A_n A_{n+1} + B_n B_{n+1} + C_n C_{n+1} + D_n D_{n+1}. \quad (6)$$

The phase retardation between two neighboring pixels  $\Delta$  will be used for the birefringence image.

For the optical axis orientation  $\theta_{n+1}$  it is impossible to obtain a solution unless changes in the polarization state in the fiber and the optical axis orientations of all previous layers are taken into account. Fortunately, we find a parameter—the difference in optical axis orientations between two neighboring layers—that can present the optical axis information. On the basis of Eq. (1), the round-trip quaternion of the  $n$ th and the  $(n + 1)$ th layers  $q_n q_{n+1}^2 q_n$  can be obtained.  $q_n q_{n+1}^2 q_n$  represents an equivalent linear phase retarder, of which the real part is

$$\begin{aligned} \text{Re}(q_n q_{n+1}^2 q_n) &= \cos(\Delta_n + \Delta_{n+1}) \\ &+ (1 - \cos 2\beta_n) \sin \Delta_n \sin \Delta_{n+1}, \end{aligned} \quad (7)$$

where  $\beta_n = \theta_{n+1} - \theta_n$  is the difference in optical axis orientations between the  $n$ th and  $(n + 1)$ th layers. The phase retardation of this equivalent retarder  $\Delta_{n,n+1}$  can also be calculated with round-trip quaternions  $Q_{T,n-1}$  and  $Q_{T,n+1}$ :

$$\begin{aligned} \cos \Delta_{n,n+1} &= A_{n-1} A_{n+1} + B_{n-1} B_{n+1} \\ &+ C_{n-1} C_{n+1} + D_{n-1} D_{n+1}. \end{aligned} \quad (8)$$

Since Eqs. (7) and (8) should be equal, we find

$$\cos 2\beta_n = 1 - \frac{\cos \Delta_{n,n+1} - \cos(\Delta_n + \Delta_{n+1})}{\sin \Delta_n \sin \Delta_{n+1}}. \quad (9)$$

We denote the image based on the  $\beta_n$  value as the differential optical axis orientation image.

Figure 1 shows the single-mode fiber-based PS-OCT system. In the reference arm a four-step driving function is applied to the polarization modulator, and each step introduces a  $\pi/4$  phase shift. Since only vertical linearly polarized light can pass the phase modulator, four different reference polarization states before the polarization modulator are selected, each separated by  $45^\circ$  angles over a great circle on a Poincaré sphere.

The four corresponding polarization states scattered from the sample arm are obtained by phase-resolved processing of the interference fringe signals obtained from two perpendicular polarization detection channels. The rotation quaternions (i.e., both the rotation axis and angle) are calculated as follows: For each pixel, three pairs of polarization states, i.e., 1 and 2, 2 and 3, and 3 and 4, are selected to calculate the rotation angles. For each pair of polarization states the relative position of the normalized Stokes vectors should be maintained in the Poincaré sphere after rotation in the absence of diattenuation. However, there is a small shift in the measured data. Suppose the angles between the initial and final polarization states are  $\varphi$  and  $\varphi'$ , respectively, and  $\delta$  is the angle difference ( $\delta = \varphi - \varphi'$ ). Both  $\varphi$  and  $\varphi'$  are modified by  $\varphi - (\delta/2)$  [i.e.,  $\varphi' + (\delta/2)$ ] by shifting all four Stokes vectors by the angle  $\delta/4$  in different directions, as shown in Fig. 2. The relationships among these vectors are as follows:

$$\begin{aligned} \mathbf{1}_{\text{new}} &= \frac{\sin[\varphi - (\delta/4)]}{\sin \varphi} \mathbf{1} + \frac{\sin(\delta/4)}{\sin \varphi} \mathbf{2}, \\ \mathbf{2}_{\text{new}} &= \frac{\sin(\delta/4)}{\sin \varphi} \mathbf{1} + \frac{\sin[\varphi - (\delta/4)]}{\sin \varphi} \mathbf{2}, \\ \mathbf{1}'_{\text{new}} &= \frac{\sin[\varphi' + (\delta/4)]}{\sin \varphi'} \mathbf{1}' - \frac{\sin(\delta/4)}{\sin \varphi'} \mathbf{2}', \\ \mathbf{2}'_{\text{new}} &= \frac{\sin(\delta/4)}{\sin \varphi'} \mathbf{1}' + \frac{\sin[\varphi' + (\delta/4)]}{\sin \varphi'} \mathbf{2}'. \end{aligned} \quad (10)$$

An exact rotation quaternion can be obtained with these shifted Stokes vectors. The average of the three

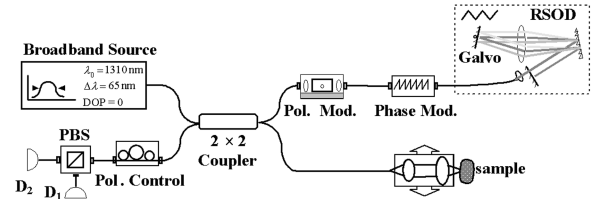


Fig. 1. Fiber-based PS-OCT system. DOP, degree of polarization; Pol. Mod., polarization modulator; Pol. Control, polarization controller; Phase Mod., phase modulator; PBS, polarization beam splitter; RSOD, rapid scanning optical delay line;  $D_1$ ,  $D_2$ , detectors.

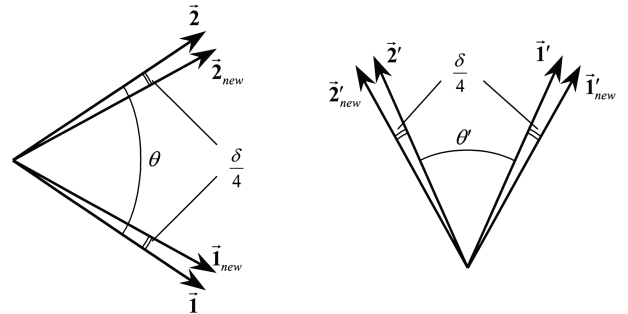


Fig. 2. Schematic diagram for shifting the Stokes vectors.  $\mathbf{1}$  and  $\mathbf{2}$  are two initial Stokes vectors.  $\mathbf{1}'$  and  $\mathbf{2}'$  are two final Stokes vectors. The vectors without subscript “new” represent Stokes vectors before shifting; those with subscript “new” represent Stokes vectors after shifting.

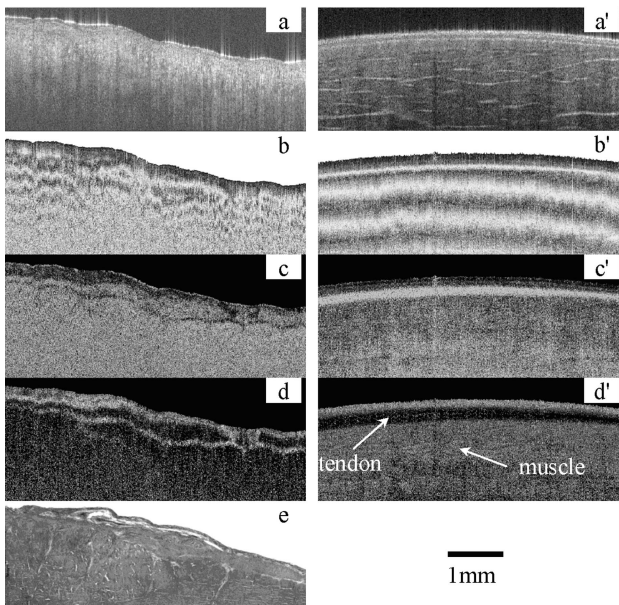


Fig. 3. PS-OCT images of a–d, beef tendon and a'–d', rabbit tendon and muscle. a, a', OCT structural images; b, b', round-trip phase retardation images; c, c', birefringence images; d, d', differential optical axis orientation images; e, histology image of beef tendon.

rotation angles obtained from the three pairs of polarization states is used as the final result.

Figure 3 shows the PS-OCT images of beef tendon (Figs. 3a–3d) and rabbit muscle and tendon (Figs. 3a'–3d'), respectively. Figures 3b and 3b' are round-trip phase retardation images that are calculated based on the assumption of a constant optical axis and do not represent the local structure of the sample. Figures 3c and 3c' are birefringence images, in which a bright area represents a strongly birefringent region, whereas a dark area represents a weakly birefringent region. Figures 3d and 3d' are differential optical axis orientation images, in which a dark area represents a region with constant optical axis, whereas a bright line represents the boundary between two adjacent birefringent layers with different optical axes. Three special cases need to be explained as follows: (1) The boundary between two neighboring birefringent layers with different optical axes is represented by a dark line in the birefringence image. This is because the boundary region is composed of two layers, and the equivalent birefringence is smaller than either layer. This is clearly shown in Fig. 3c, in which the dark line is the boundary region between two layers of tendon with different optical axis orientations. (2) A region without birefringence is represented as a very dark area in the birefringence image. However, the same region will appear as a bright area in the differential optical axis orientation image. This is because the denominator in Eq. (9) is close to zero, and thus little noise will result in a large  $\beta_n$  value. This is confirmed in Fig. 3d, in which the left-side upper layer of the tissue represents a zero birefringence layer. (3) One of the limitations of our current analysis is that we consider only a linear phase retarder model. An elliptical phase

retarder model that includes diattenuation will be considered in future work. A preliminary analysis indicates that the layer, which should be modeled with an elliptical phase retarder, will appear as a medium-bright area in the differential optical axis orientation image due to this limitation. The muscle layer in Fig. 3d' gives such an example. Histology of the beef tendon (Fig. 3e) is included for comparison. A clear boundary can be found in Figs. 3c–3e, but not in the conventional OCT structural image (Fig. 3a). It is obvious that, in addition to the conventional OCT structural image, birefringence and differential optical axis orientation images can provide more detailed information, especially boundaries between different layers. The axial resolution of the structural image is  $10\ \mu\text{m}$ . The birefringence and differential axis images are calculated with a convolution of 5 pixels to reduce the effect of the speckle noise. The A-line scanning frequency is 500 Hz, and the data processing time of a  $1\ \text{mm} \times 2\ \text{mm}$  imaging area is less than 1 s.

In summary, previous PS-OCT research focused on round-trip phase retardation and Stokes parameter imaging. However, it cannot provide specific birefringence information on layers with different optical axes. The novel depth-resolved birefringence and differential optical axis orientation imaging technique reported here can distinguish local birefringent structures in different layers, therefore providing better image contrast for multiple-layer samples.

Thanks to Angela Liogys for help with the histology. This work was supported by research grants awarded by the National Science Foundation (BES-86924) and the National Institutes of Health (EB-00293, EB-00255, EB-002495, NCI-91717, RR-01192, and AR-47751). Institutional support from the Air Force Office of Scientific Research (F49620-00-1-0371) and the Beckman Laser Institute Endowment is also gratefully acknowledged. Please address all correspondence to Zhongping Chen at zchen@bli.uci.edu.

## References

1. D. Huang, E. A. Swanson, C. P. Lin, J. S. Schuman, W. G. Stinson, W. Chang, M. R. Hee, T. Flotte, K. Gregory, C. A. Puliafito, and J. G. Fujimoto, *Science* **254**, 1178 (1991).
2. M. R. Hee, D. Huang, E. A. Swanson, and J. G. Fujimoto, *J. Opt. Soc. Am. B* **9**, 903 (1992).
3. J. F. de Boer, T. E. Milner, M. J. C. van Gemert, and J. S. Nelson, *Opt. Lett.* **22**, 934 (1997).
4. C. E. Saxer, J. F. de Boer, B. H. Park, Y. Zhao, Z. Chen, and J. S. Nelson, *Opt. Lett.* **25**, 1355 (2000).
5. S. Jiao and L. V. Wang, *Opt. Lett.* **27**, 101 (2002).
6. H. Ren, Z. Ding, Y. Zhao, J. Miao, J. S. Nelson, and Z. Chen, *Opt. Lett.* **27**, 1702 (2002).
7. J. F. de Boer and T. E. Milner, *J. Biomed. Opt.* **7**, 359 (2002).
8. C. K. Hitzenberger, E. Götzinger, M. Sticher, M. Pircher, and A. F. Fercher, *Opt. Express* **9**, 780 (2001), <http://www.opticsexpress.org>.
9. S. Jiao and L. V. Wang, *J. Biomed. Opt.* **7**, 350 (2002).
10. S. Jiao and L. V. Wang, *OE Mag.* **3**(7), 20 (2003).
11. M. Richartz and H. Hsu, *J. Opt. Soc. Am.* **39**, 136 (1949).